Computational Study of the Blood Flow in Three Types of 3D Hollow Fiber Membrane Bundles

Jiafeng Zhang
Xiaobing Chen
Jun Ding
Katharine H. Fraser[2]
M. Ertan Taskin[3]
Bartley P. Griffith
Zhongjun J. Wu[1]

Artificial Organs Laboratory,
Department of Surgery,
University of Maryland School of Medicine
Baltimore, MD 21201
e-mail: zwu@smail.umaryland.edu

The goal of this study is to develop a computational fluid dynamics (CFD) modeling approach to better estimate the blood flow dynamics in the bundles of the hollow fiber membrane based medical devices (i.e., blood oxygenators, artificial lungs, and hemodialyzers). Three representative types of arrays, square, diagonal, and random with the porosity value of 0.55, were studied. In addition, a 3D array with the same porosity was studied. The flow fields between the individual fibers in these arrays at selected Reynolds numbers (Re) were simulated with CFD modeling. Hemolysis is not significant in the fiber bundles but the platelet activation may be essential. For each type of array, the average wall shear stress is linearly proportional to the Re. For the same Re but different arrays, the average wall shear stress also exhibits a linear dependency on the pressure difference across arrays, while Darcy's law prescribes a power-law relationship, therefore, underestimating the shear stress level. For the same Re, the average wall shear stress of the diagonal array is approximately 3.1, 1.8, and 2.0 times larger than that of the square, random, and 3D arrays, respectively. A coefficient C is suggested to correlate the CFD predicted data with the analytical solution, and C is 1.16, 1.51, and 2.05 for the square, random, and diagonal arrays in this paper, respectively. It is worth noting that C is strongly dependent on the array geometrical properties, whereas it is weakly dependent on the flow field. Additionally, the 3D fiber bundle simulation results show that the three-dimensional effect is not negligible. Specifically, velocity and shear stress distribution can vary significantly along the fiber axial direction. [DOI: 10.1115/1.4025717]

Keywords: artificial lung, hollow fiber, shear stress, computational fluid dynamics, microscale modeling

1 Introduction

Hollow fiber membrane bundles are commonly used in blood-contacting medical devices for replacement of human organ functions or treatment of diseases. Lung assist devices, also known as blood oxygenators or artificial lungs, are medical devices designed to replace or supplement the respiratory function of lungs. They are routinely used in cardiopulmonary bypass for open heart surgery and for extracorporeal membrane oxygenation with cardiac/cardiopulmonary supports [1]. Blood oxygenation in artificial lungs is a diffusion process between blood and oxygen, usually achieved with the aid of hollow fiber membranes. In these devices, blood flows around the outside of thousands of hollow fibers, and oxygen flows inside the fiber lumen [2,3]. Hemodialysis is a clinical approach that is also based on diffusion to remove metabolic waste products (i.e., potassium, urea and inorganic salt, etc.), as well as excessive free water, from blood when patients have renal failure [4]. These devices have benefitted many patients; however, there are still a number of complications and problems associated with these devices. For example, device-induced blood trauma (i.e., hemolysis, platelet activation, and alteration of blood coagulation) and thrombosis are important issues limiting device performance and are clinical complications.

Mechanisms of blood damage in hollow fiber membrane bundles are complicated and have not been well investigated. In general, they are related to the internal architecture of devices, biocompatibility of device materials, and local flow dynamics. The quantitative study of the effect of hollow fiber bundle structure/packing on mass transfer and device-induced blood trauma remains challenging because blood flow in the hollow fiber bundle is complicated and difficult to measure [5]. Generally, empirical design and in vitro testing are adopted to evaluate the overall performance of oxygenators and hemodialyzers [6–8], which could not provide flow details and mass transport processes inside the hollow fiber bundle for relating the device design to its performance and clinical complications.

Recently, interests in fluid dynamics inside fiber bundle devices have led to the development of CFD models that provide some useful methods to estimate flow, mass, and heat transport phenomena [2,3,9–20]. Some of these models [2,3,9–13] assumed fiber bundles as homogeneous porous media, and blood flow through fiber bundles was numerically solved using multiphase fluid dynamics. Flow properties were volume averaged with lumped parameters. The superficial fluid velocity or interstitial velocity was estimated by the flow rate, cross-sectional area, permeability, and porosity. These models could capture global flow patterns and some flow properties through membrane bundles and have proven to be capable of modeling the overall device performance in a relatively efficient way. However, these models could not provide detailed local flow characteristics inside the fiber bundles. Specifically, local velocity distributions and local shear stress

[1]Corresponding author.
[2]Current address: Fraser K. H., Department of Bioengineering, Imperial College London, London, UK.
[3]Current address: Taskin M. E., HeartWare Inc., 14000 NW 57th, Court, Miami Lakes, FL 33014

Contributed by the Bioengineering Division of ASME for publication in the Journal of Biomechanical Engineering. Manuscript received January 11, 2013; final manuscript received October 10, 2013; accepted manuscript posted October 19, 2013; published online November 6, 2013. Assoc. Editor: Dalin Tang.

distributions around individual fibers are not available to accurately predict blood damage and thrombotic potential in devices.

On the other hand, heterogeneous models or so-called microscale models were also developed [14–20]. These microscale models were mainly in two categories: (1) blood flow and mass transfer around a single fiber [14,15] or (2) the interstitial blood flow and mass transfer among fiber arrays [16–20]. Mazaheri and Ahmadi [19] computationally studied a 2D oxygenator with a diagonal array of 3300 hollow fibers, and they reported that the blood flow inside the fiber bundle was nonuniform, which is different from the uniform flow predicted by the porous media model. They also pointed out that pseudohomogeneous porous models may not be able to correctly predict the transport properties, such as the residency time.

In spite of numerous studies of hollow fiber bundles, many key factors affecting oxygenator performances are still not well understood. For example, all the previously discussed computational studies focused on either a single fiber or arrays of identical fibers with uniform patterns perpendicular to the flow. However, hollow fibers in oxygenators are neither in nice uniform patterns nor identical. Distances between fibers may vary; cross sections of fibers may be different; fibers may not be perpendicular to the coming flow [21,22]. Furthermore, the local shear stress distributions have not yet been studied, which is important to estimate the shear-induced blood damage. Flow entrance and exit effects may be significant, and the non-Newtonian viscosity (shear thinning) of blood may need to be considered to better understand the local shear stress distributions [23,24].

The aim of this study is to develop a microscale CFD modeling approach to better understand blood flow in hollow fiber bundles for artificial lung devices and hemodialyzers. The relationship between shear stress distribution and the types of fiber arrays was the primary interest of this paper. Three types of arrays (square, diagonal, and random) were chosen to represent fiber configurations.

2 Materials and Methods

Fiber bundles in oxygenators or hemodialyzers are usually made from fiber sheets of evenly spaced fibers. Thus, the fibers in a bundle are evenly spaced in the lateral direction. The space between two layers may be varied and arranged according to the fiber bundle porosity, which is defined as the ratio of void space and total volume of the bundle. In this study, four types of fiber arrays with a porosity of 0.55 were created (Fig. 1). Fibers in the square (Fig. 1(*a*)), diagonal (Fig. 1(*b*)), and random (Fig. 1(*c*)) arrays are parallel to each other, while angles between the odd and even row fibers in the 3D array are at 20 deg (Fig. 1(*d*) and the insert). Polypropylene fibers prearranged in a sheet format of 50 fibers per inch (Celgard® X30-240, Celgard, NC) were used in these models. In the square model, the distance between two neighboring fibers along the *Y*-direction is 508 μm, consist with the fiber sheet format; the fibers in the *X*-direction are in parallel lines with a distance of 314 μm (Fig. 1(*a*)). For the diagonal bundle, the distance between two neighboring fibers along the *Y*-direction remains to be 508 μm. However, the fibers in the *X*-direction is shifted 254 μm in the *Y*-direction relative to neighboring fibers and the distance in the *X*-direction remains to be 314 μm (Fig. 1(*b*)). For the random array, a series of random values generated with the random function (Matlab, Mathwork, MA) were used to determine the relative positions of fiber layers (Fig. 1(*c*)). These models replicate a block of the fiber bundles. The first two models represent the two extreme configurations while the random model may represent a typical configuration of an artificial lung. The 3D model was generated by rotating the odd row fibers of the square array by 10 deg and the even row fibers by 10 deg in the opposite direction (Fig. 1(*d*)). The angle between the odd and even row fibers was selected according to the measurement of the fiber bundle in the Thoratec pediatric pump lung device (Thoratec Corporation, Pleasanton, CA). A schematic presentation of the model and corresponding mesh structure of the diagonal array are shown in Fig. 2. The computational domain was composed of 216 fibers, an inflow section before, and an outflow section after the bundle inside a cuboid domain. The bundle was located at the middle of the domain to avoid the inlet and outlet boundary effects. Uniform velocities at the inlet and outlet were selected to define the fluid advection. The top, bottom, and two side walls were set as symmetry walls. No-slip wall conditions were applied along the fiber walls.

Mesh independence analysis was conducted, and the final mesh of the flow domain contained 3.5 to 4.3 $\times 10^6$ hybrid (tetrahedral/hexahedral) elements. Structured hexahedral elements were used for the inflow and outflow regions, and finer meshes were generated in the fiber array region. Fine hybrid elements were utilized in the area adjacent to hollow fibers (Fig. 2(*b*)). All the computational models were implemented and meshed with a commercial geometry and mesh development software Gambit v.2.4.6 (Ansys Fluent Inc., Lebanon, NH). The commercial CFD simulation software Fluent 13.0 (Ansys Fluent Inc., Lebanon, NH) was used to compute the interstitial blood flow through the fiber arrays. The blood flow was assumed to be steady and incompressible. Given the low Reynolds number, the laminar model was utilized to solve the continuum and momentum equations [14–18,21,22]

$$\nabla \cdot \vec{v} = 0 \tag{1}$$

$$\rho\left(\frac{\partial \vec{v}}{\partial t} + \vec{v} \bullet \nabla \vec{v}\right) = -\nabla p + \nabla \cdot \bar{\tau} \tag{2}$$

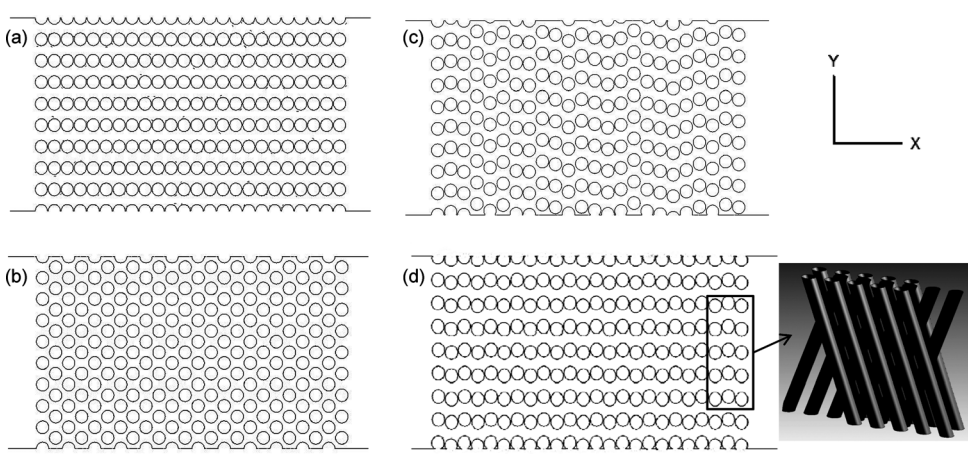

Fig. 1 Schematic top views of the (*a*) square, (*b*) diagonal, (*c*) random, and (*d*) 3D arrays. Each array has 216 hollow fibers and the porosity is 0.55. The insert shows the 3D fibers.

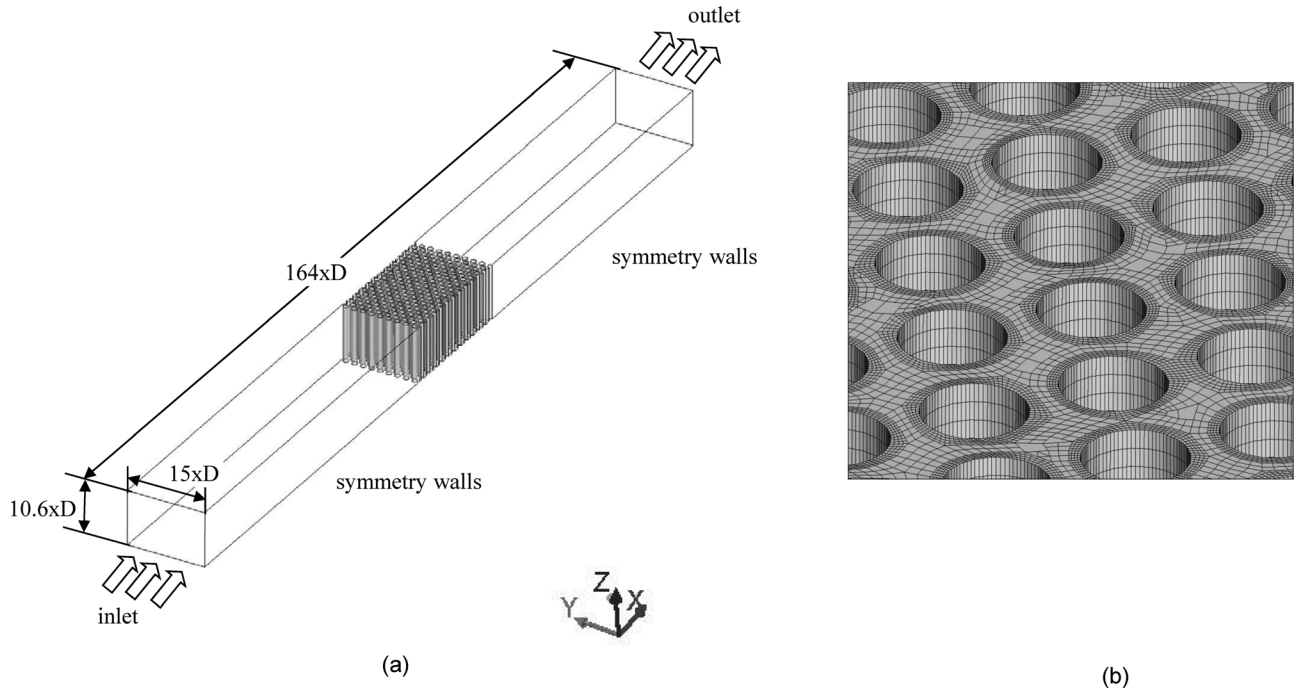

Fig. 2 (*a*) CFD geometry and (*b*) mesh illustrations around the fibers for the diagonal array

where $\vec{v}$ is the velocity vector, ρ is the density of the blood, $\bar{\tau}$ is the stress tensor, and p is the pressure. $\bar{\tau}$ is linearly dependent on the rate of deformation tensor $\mathbf{D}$, $\bar{\tau} = 2\mu\mathbf{D}$, where $\mathbf{D} = (\nabla \boldsymbol{v} + \nabla \boldsymbol{v}^T)/2$.

Blood was approximated as a non-Newtonian fluid with shear rate dependent on the fluid viscosity as given by the following modified Casson model [20,25]:

$$\mu = \left(\left(\frac{\tau_0}{\varphi + 1} \right)^{1/2} + \mu_c^{1/2} \right)^2 \tag{3}$$

where τ_0 is the yield stress and the value was 0.005 Pa; φ is the magnitude of the shear rate, and μ_c is the Casson viscosity and the value is 3.5 cP for human blood. ρ is the blood density, which is 1056 kg/m^3 for human blood.

The semi-implicit method for pressure-linked equations (SIMPLE) pressure-velocity coupling algorithm was utilized and all discretizations were performed with second-order accuracy. A user-defined function was utilized to implement the non-Newtonian blood flow property in the model. Solutions were judged to be numerically converged when all four (continuity and three velocity components) scaled residuals were smaller than 1×10^{-5}.

Reynolds numbers (Re) 1.0, 5.0, and 10.0 were selected. This Re range is representative for realistic situations encountered in artificial lungs as previously reported [20]. Re measures the ratio of the inertial to the viscous flow effects for the flow domain and is defined as the following [20]:

$$\mathrm{Re} = \frac{U_{\mathrm{in}} D \rho}{\mu_c} \tag{4}$$

where U_{in} is the average inlet velocity, and D is the diameter of the hollow fibers.

Permeability of the porous bundle is calculated as the following [26,27]:

$$K_p = \frac{\mu_c (Q/A)}{\Delta p / l} \tag{5}$$

where Q is the inlet flow rate, A is the cross-sectional area perpendicular to the flow direction, Δp is the pressure difference across the fiber bundle, and l is the bundle length in the flow direction. An average wall shear stress over the cylindrical array by interstitial flows is theoretically derived and estimated as the following [27,28]:

$$\tau_{\mathrm{av}} = \frac{4}{\pi} \frac{\mu_c (Q/A)}{\sqrt{K_p}} \tag{6}$$

The pressure drop in Eq. (5) is usually obtained from the experimental measurements in macroscale analysis. However, it was obtained from the simulation in this study for the purpose of comparing the simulated shear stress by the microscale models with the analytical estimate on the fiber bundles in this paper. Equations (5) and (6) together provide the analytical estimate of the average shear stress in a homogenous porous media. However, the average shear stress estimated from Eqs. (5) and (6) does not incorporate the impact of the geometrical configuration of fiber arrays, such as fiber spatial distribution and fiber diameter. In the following section, simulation results are compared with the analytical estimate by Eqs. (5) and (6) for different Reynolds numbers (Re = 1.0, 5.0, and 10.0) and different fiber array geometrical configurations.

3 Results

Figure 3 shows the velocity magnitude contours at selected cross sections for the square, diagonal, random, and 3D fiber arrays when Re is 5.0. As expected, the blood velocity increases after the blood enters the fiber bundle because the flow area decreased. Velocities are nonuniformly distributed in fiber bundles. The peak velocities are approximately 0.18, 0.22, 0.33, and 0.27 m/s for the square, diagonal, random, and 3D arrays, respectively. The nonuniform distribution of the velocity fields is consistent with what Mazaheri and Ahmadi reported in 2006 [19], and this indicates the irregular local shear stress distributions. Figures 3(*d*)–3(*f*) show a strong three-dimensional effect in the velocity field of the 3D array. Specifically, the velocity distribution varies significantly in the z direction (in other words, along the

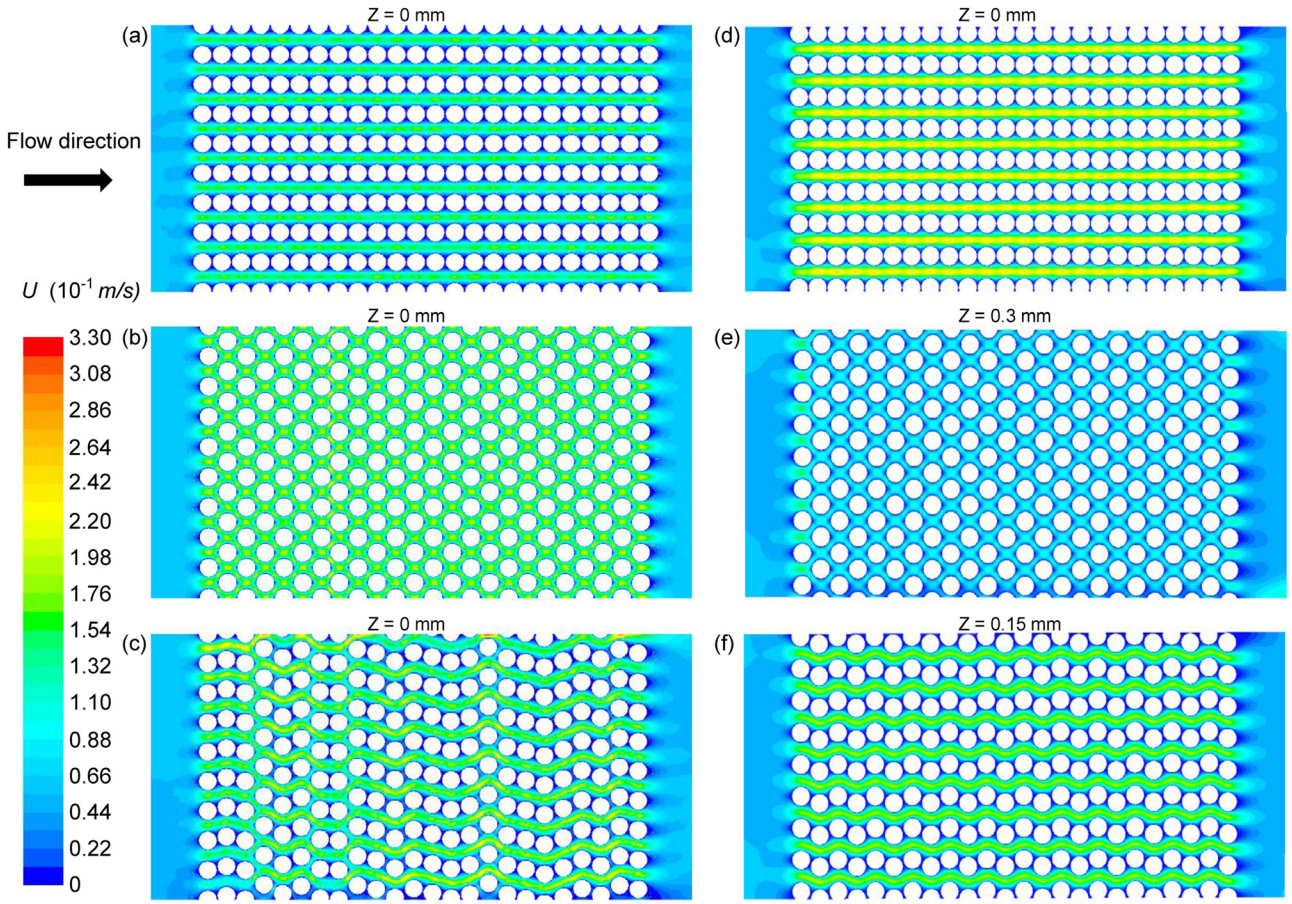

Fig. 3 Contours of velocity magnitude (m/s) around fibers at selected cross sections for the (*a*) square, (*b*) diagonal, (*c*) random, and (*d–f*) 3D arrays when Re is 5.0

fiber axis direction). It is worth noting that the velocity magnitudes plotted in Fig. 3 include all three components, and a direct comparison of Figs. 3(*a*) and 3(*d*) (or 3(*b*) and 3(*e*)) is not relevant.

The representative velocity fields around the fibers in these three fiber arrays are depicted in Fig. 4 (Re = 5.0). For the square array (Fig. 4(*a*)), larger velocities were seen in the side gaps between the fiber rows along the flow direction, and smaller velocities were seen in the gaps between the fiber columns perpendicular to the flow direction. For the diagonal array (Fig. 4(*b*)), velocities were relatively evenly distributed around fibers. For the random array (Fig. 4(*c*)), velocities varied significantly at different locations (i.e., around fibers in the back (fiber c1), front (fiber c2), or side regions (fiber c3)).

Shear stress contours in the square, diagonal, and random arrays are presented in Fig. 5 (Re = 5.0). On average, the diagonal array had the highest shear stresses, and the square array had the lowest shear stresses. The average shear stress in the random array lied in between. Wall shear stresses for select fibers from these three fiber arrays are presented in Figs. 5(*d*)–5(*f*). Similarly, the square array showed the lowest wall shear stress. The wall shear stress distribution is approximately the same for every individual fiber in both square and diagonal arrays due to their symmetric geometry. However, wall shear stresses varied significantly from one fiber to another in the random array (refer to fibers 1 to 8 in Fig. 5(*f*)). The peak local wall shear stresses were 21.80, 45.98, and 52.58 Pa for the square, diagonal, and random arrays, respectively.

Figure 6 shows the shear stress contours in the 3D array when Re is 5.0. Similar to the velocity field that was presented previously, shear stress varies significantly in the z direction as well. The three-dimensional effect is more obvious in the wall shear stress contour shown in Fig. 6(*d*). The peak wall shear stress is approximately 26.93 Pa, which appears at the squarelike cross sections (Fig. 6(*a*)).

Wall shear stress distributions for select fibers (Re = 5.0) are presented in Fig. 7. For the square and diagonal arrays (Figs. 7(*a*) and 7(*b*)), wall shear stresses are symmetrical with respect to the flow direction (or X direction) for each fiber. However, wall shear stresses are asymmetrical for the random array (fibers c1, c2, and c3 in Fig. 7(*c*)), especially for the fiber c3. It can be shown that this asymmetrical wall shear stress distribution could decrease the potential of platelet deposition. Because of the non-Newtonian shear thinning behavior of the blood [23,24], wall shear stress may contain a component normal to the front wall that points towards the fiber walls (i.e., Figs. 7(*b*) and 7(*c*)).

Figure 8 shows the area-weighted average wall shear stresses over the fibers in one row along the flow direction when Re is 5.0 (Fig. 8(*a*)) and the global area-weighted average shear stress over all 216 fibers for different Re (Fig. 8(*b*)). For all the selected Re, the diagonal array has the highest average shear stress; the square array has the lowest average shear stress; the average shear stress of the random array and 3D array fall in the middle (Fig. 8(*b*)). Interestingly, for the square, diagonal and 3D arrays, the average shear stresses over the individual fibers are approximately the same, except the fibers in the first and last columns. These differences reflect the effects of the flow fields at the entrance (the first column) and the exit (the last column) where the flow fields are very different from those in the middle section. On the contrary, the average shear stresses for the individual fibers in the random array vary randomly (Fig. 8(*a*)). The average wall shear stresses of the random and 3D arrays are very close.

Figure 9 presents the probability density function (PDF) of the global wall shear stresses on the 216 fibers in the four arrays, respectively. The PDF describes the relative possibility for a

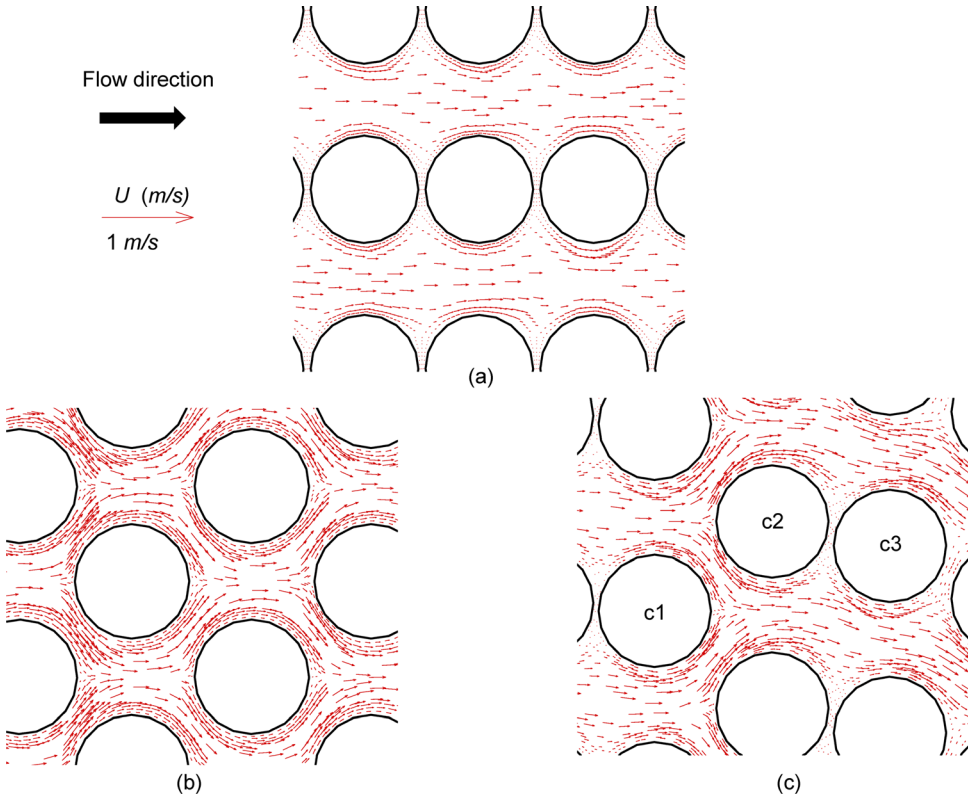

Fig. 4 Flow velocity vectors around selected fibers at a middle cross section for the (*a*) square, (*b*) diagonal, and (*c*) random arrays when Re is 5.0

random variable to take on a given value. The PDF is always larger than or equal to 0, and its integral over the entire space is equal to 1. For the square array (Fig. 9(*a*)), the wall shear stresses range from 0 to 21.8 Pa, and approximately 40% of the wall surfaces has shear stress smaller than 1.0 Pa. The PDF of the square array remains a relatively low value (i.e., $< 4\%$) for the wall shear stresses larger than 1.0 Pa. On the contrary, the wall shear stresses vary in much wider ranges for the diagonal and random arrays. For the diagonal array (Fig. 9(*b*)), wall shear stresses are between 0 and 46.0 Pa. Different from the square array, less than 1% of the wall surface in the diagonal array has the shear stresses smaller than 1.0 Pa, and over 80% of the wall surface has the shear stresses larger than 15.0 Pa. Most of the wall surface has the wall shear stresses between 15.0 Pa and 30.0 Pa. For the random array (Fig. 9(*c*)), wall shear stresses spread over a wide range from 0 to 40.0 Pa. Different from the diagonal and square arrays, approximately 9% of the wall surface has wall shear stresses smaller than 1.0 Pa, and the overall distribution is relatively flat. For the 3D array (Fig. 9(*d*)), wall shear stresses also spread over a wide range. Approximately 7% of the wall surface has wall shear stresses smaller than 1.0 Pa.

Table 1 lists the maximum, median, and area-weighted average shear stresses of the four arrays when Re varies from 1.0 to 10.0. For the same Re, the random array has the largest maximum wall shear stress and the square array has the smallest maximum wall shear stress. However, the diagonal array has much larger median and mean shear stresses than other arrays. Specifically, for the same Re, the average wall shear stress of the diagonal array is approximately 3.1, 1.8, and 2.0 times larger than that of the square, random, and 3D arrays, respectively. It is worth noting that the area-weighted average wall shear stresses are linearly proportional to the Re for each type of array, which indicates that the Darcy permeability is weakly dependent on the flow field (see Eqs. (5) and (6)).

In Fig. 10, the simulated global average wall shear stresses for the square, diagonal and random arrays were grouped by Re and compared with the analytical solutions (see Eq. (6)). The solid lines show the results of $\mathrm{Re} = 10.0$; the dashed lines show the results of $\mathrm{Re} = 5.0$; the dotted lines show the results of $\mathrm{Re} = 1.0$. The lines in black represent the results of simulations, whereas the lines in gray indicate the analytical results derived from Eq. (6). The diamond, triangular, and square symbols refer to the diagonal array, the random array, and the square array, respectively. For each Re, when the spatial configuration of fiber arrays changed from the square array (square symbols in Fig. 10) to the random array (triangular symbols in Fig. 10) to the diagonal array (diagonal symbols in Fig. 10), the analytical solutions (gray lines) were proportional to the square root of the pressure difference (see Eqs. (5) and (6)). However, the simulated data (black lines) showed a linear relationship with an incline rate of 0.0086. Furthermore, the deviation between the simulated data (black lines) and the analytical solutions (gray lines) increased with the pressure difference across the arrays for the same Re. For example, when Re was 5.0, the relative deviation between the simulated data and the analytical solution was approximately 46% when the pressure difference across the fiber array was 745.56 Pa (square array); the relative deviation increased to approximately 91% when the pressure difference increased to 1281.28 Pa (random array); the relative deviation became approximately 160% when the pressure difference became 2348.10 Pa (diagonal array).

To estimate the potential of platelet activation, the linear stress accumulation (SA) used by Xenos et al. [29] was calculated. Approximately 1800 particles were released from the inlet, and stresses and time which particles experienced when they passed the fiber bundles were tracked; SA for each particle was then calculated by linearly integrating the shear stresses over time. The PDF of the SA is plotted in Fig. 11 for the four arrays. The PDF of the SA can be used to illustrate the overall thrombogenic potential of the blood flow [29]. The mean SA for the square, diagonal, random and 3D arrays are 0.51 Pa·s, 0.77 Pa·s, 0.48 Pa·s, and 0.55 Pa.s. The 10th percentile of the SA distribution for the square, diagonal, random, and 3D arrays are 0.17 Pa·s, 0.31 Pa·s,

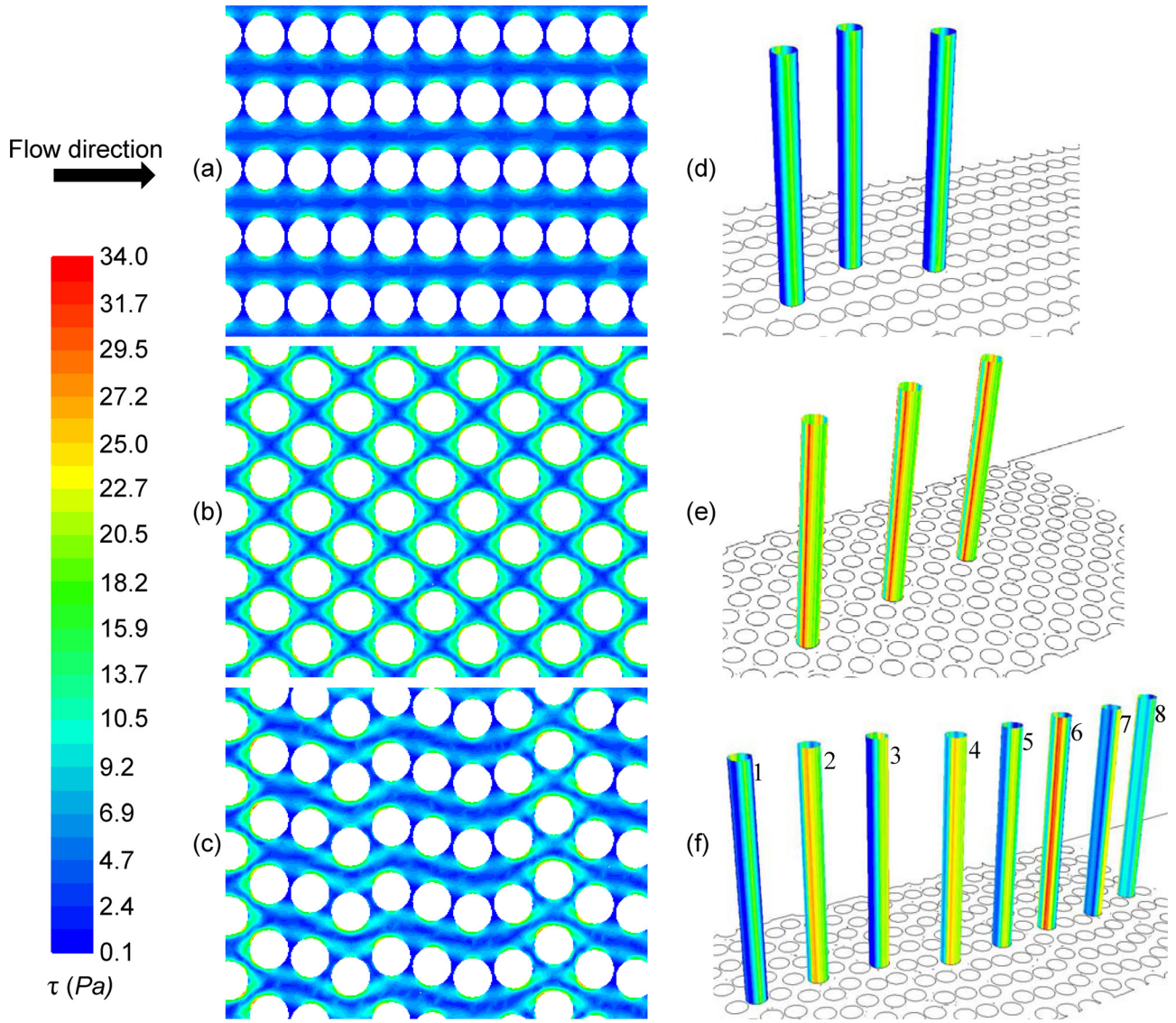

Fig. 5 Shear stress contours at the middle plane of the (*a*) square, (*b*) diagonal, and (*c*) random arrays, and wall shear stress contours on the selected fibers for the (*d*) square, (*b*) diagonal, and (*c*) random arrays when Re is 5.0

0.26 Pa·s and 0.17 Pa·s, respectively; the medians of the SA distribution for the square, diagonal, random, and 3D arrays are 0.26 Pa·s, 0.65 Pa·s, 0.37 Pa·s and 0.37 Pa.s, respectively; the 90th percentile of the SA distribution for the square, diagonal, random, and 3D arrays are 1.28 Pa·s, 1.33 Pa·s, 0.86 Pa·s and 0.93 Pa.s, respectively. SA is more widely distributed for the square, diagonal, and 3D arrays. For the random array, 80% of the SA fall in a relatively narrower region from 0.26 Pa·s to 0.86 Pa·s compared with the other types of arrays.

4 Discussion

This study aimed to build the link between the shear stresses estimated by the direct microscale CFD approach and macro approach, by which one may be able to evaluate the potential of the platelet deposition and hemolysis in the hollow fiber bundles more accurately and efficiently. Since blood is a non-Newtonian fluid with the shear thinning property, the local blood viscosity is higher where the local shear stress is smaller (see Eq. (3)). As shown in Fig. 6, the local shear stress around fibers varies significantly for the square and the random arrays, which means the local viscosity varies significantly too. For example, the largest local viscosity could be more than 20% larger than the smallest local viscosity in the square array. This shows the importance of considering the non-Newtonian viscosity of blood in this type of study.

Hemolysis can be caused by mechanical shear stress in fiber arrays. The mechanical shear stress can rupture the red blood cell membrane when it exceeds a critical threshold (∼150 Pa) [30]. Additionally, hemolysis can be caused by increasing the exposure time of red blood cells to stress lower than the threshold [30]. It has been reported that the amount of hemolysis follows a power law of shear stress magnitude and exposure time [31]. Square, diagonal, random, and 3D fiber arrays were investigated at different flow rates (or Re), and the maximum shear stresses for these arrays at the highest flow rate (i.e., Re = 10.0) are well below the critical value (∼150 Pa). Given that Re in most oxygenators is below 10.0 and the exposure time is a few seconds, hemolysis seems to be negligible inside the fiber bundles. On the other hand, platelet activation and deposition may be significant. In a recent review of previous investigations [32], Fraser et al. pointed out that both shear stress and exposure time play important roles in platelet activation. Specifically, platelets could be activated with high shear stress even with short exposure time or low shear stress if the exposure time is long enough. Since the diagonal array has higher median and mean wall shear stresses (i.e., > 40 Pa when

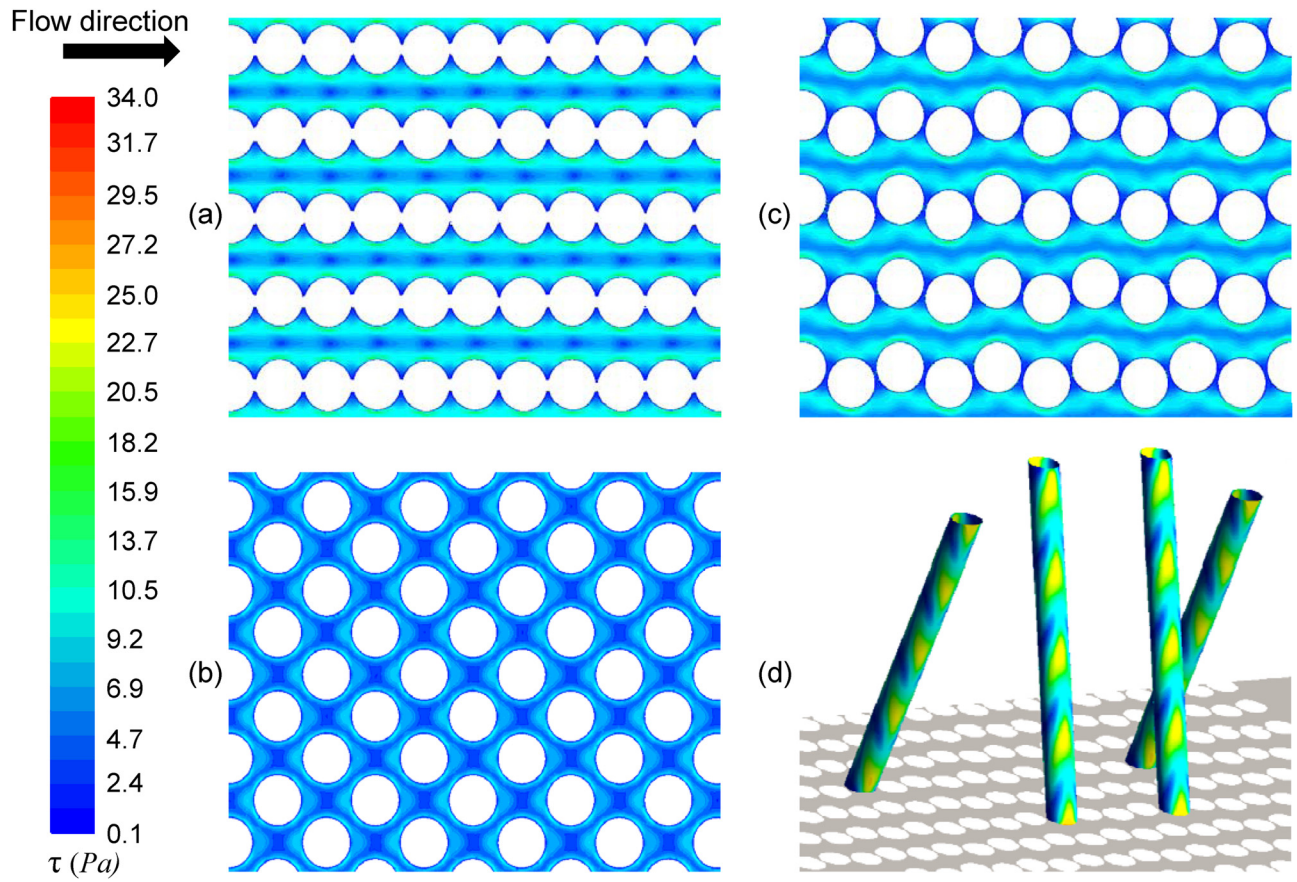

Fig. 6 Shear stress contours at the selected cross sections (*a*) $z = 0$ mm, (*b*) $z = 0.3$ mm, and (*c*) $z = 0.15$ mm, and wall shear stress contour on the selected fibers (*d*) for the 3D array when Re is 5.0

Re = 10.0), platelets have a relatively higher possibility to be activated inside the diagonal fiber bundle. However, areas with very low flow velocity in the square array could see more platelet deposition.

Some previous numerical studies of oxygenators used the homogenous porous media simplification [10,33,34] in order to reduce the computational cost. However, realistic fiber bundles are not homogenous, and the local flow details are actually important in estimating blood damage. In fact, fibers are mostly arranged in a random pattern [15,21,22], and spaces between fibers where blood flows through the fiber bundle are also different. For example, this study has demonstrated the existence of the nonuniform flow (see Figs. 3 and 4) and nonuniform shear stress (see Figs. 5 and 6) in all three directions in every type of fiber bundles. This difference between the reality and the simplified macro approach can result in nonnegligible errors in estimating the device performances and the related blood damage.

Shear stress distributions are important indicators to estimate blood damage and deposition inside the oxygenators [4,35,36]. Usually, very low shear stresses may lead to the platelet adhesion and blood clot to fiber walls [37]. On the other hand, high shear stresses could induce the platelet activation and even hemolysis, which can decrease gas exchange capacities and affect device performance. Different fiber arrangements could result in different local blood dynamics [16,17]. Larger shear rate often appears in the areas close to fiber walls, and that is why the wall shear stress distribution is of great interest. One of the criteria for good oxygenator design is to ensure the peak wall shear stress to be within the critical threshold in order to decrease the potential of blood damages [38]. Although the random array has the larger maximum shear stress than the square and diagonal arrays, the percentage of the area with the high shear stress (i.e., >40.0 Pa when Re = 5.0) is very small. Specifically, less than 2% areas have the shear stress larger than 40.0 Pa. Instead of comparing the maximum stress, the average wall shear stress better represents the global potential blood damage [39] because the average value indicates the level of the shear stress that the blood cells most likely experience.

As shown in Sec. 3, the average wall shear stress is linearly proportional to Re (Fig. 8(*b*)), which can be predicted by the analytical solution of Eq. (4), (5), and (6) through simple algebra. This linear relationship was also reported in the previous microscale flow modeling in three-dimensional porous scaffold [35,36]. It is worth noting that Eq. (6) is derived from Darcy's law for homogeneous porous media, which assumes the viscous force term ($\nabla^2 u$) is negligible outside the very thin boundary layer (thickness $\sim O(\sqrt{K_p}/D)$ [28]. In other words, K_p/D^2 should be much smaller than 1. Results show that the pressure difference across the arrays has negligible dependence on Re but strong dependence on the geometrical configurations of arrays (i.e., the volume fraction), which explains why Eq. (6) predicts the linear relationship between the average wall shear stress and Re for each type of the arrays (see Fig. 8(*b*)) but not the linear relationship between the average wall shear stress and the pressure difference across arrays (see Fig. 10).

However, quantitatively, the analytical estimation of the average wall shear stress by Eq. (6) significantly deviates from that predicted by the CFD modeling (see Fig. 10), especially when the pressure difference increases. As discussed previously, the viscous force term ($\nabla^2 u$) cannot be neglected if K_p/D^2 is comparable to 1. For the arrays studied in this paper, K_p calculated by the CFD model is on the order of 10^{-10} to 10^{-9}, and the fiber diameter is approximately on the order of 10^{-4}, from which one can derive that K_p/D^2 is on the order of 10^{-1} to 1. Apparently, the viscous

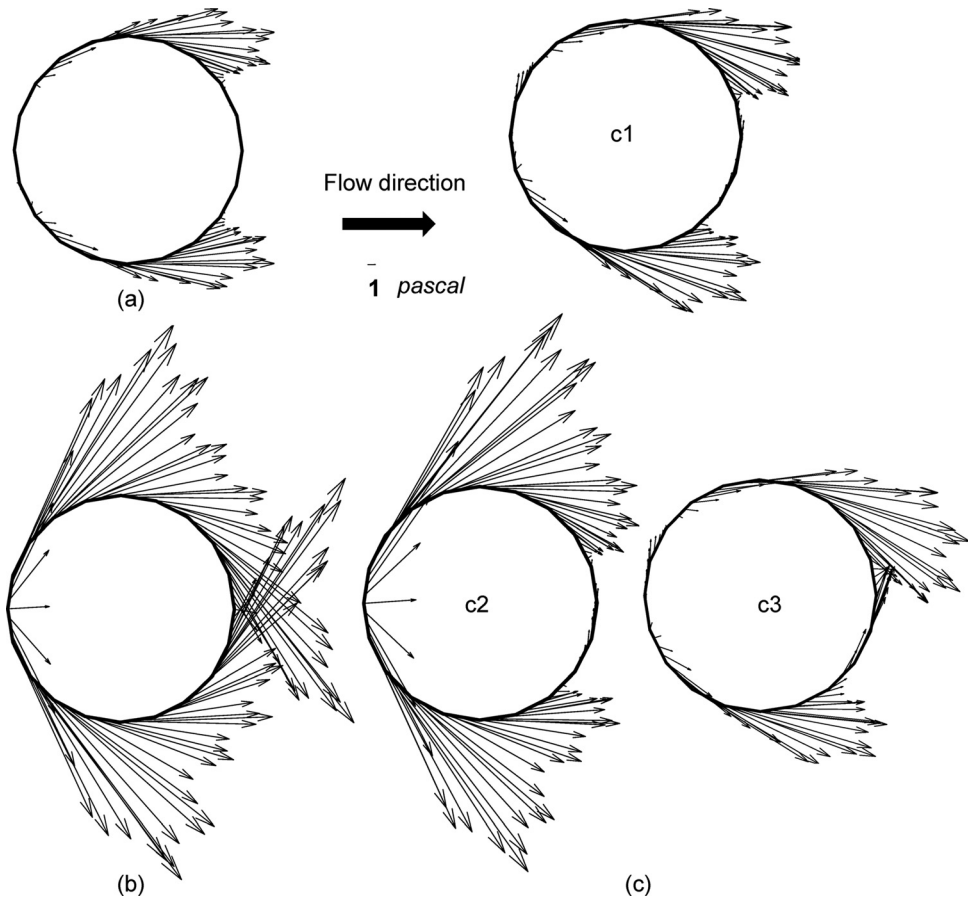

Fig. 7 Wall shear stress vectors (*X*- and *Y*- shear stresses only) at the *X*-*Y* plane for the selected fibers for the (*a*) square, (*b*) diagonal, and (*c*) random arrays when Re is 5.0

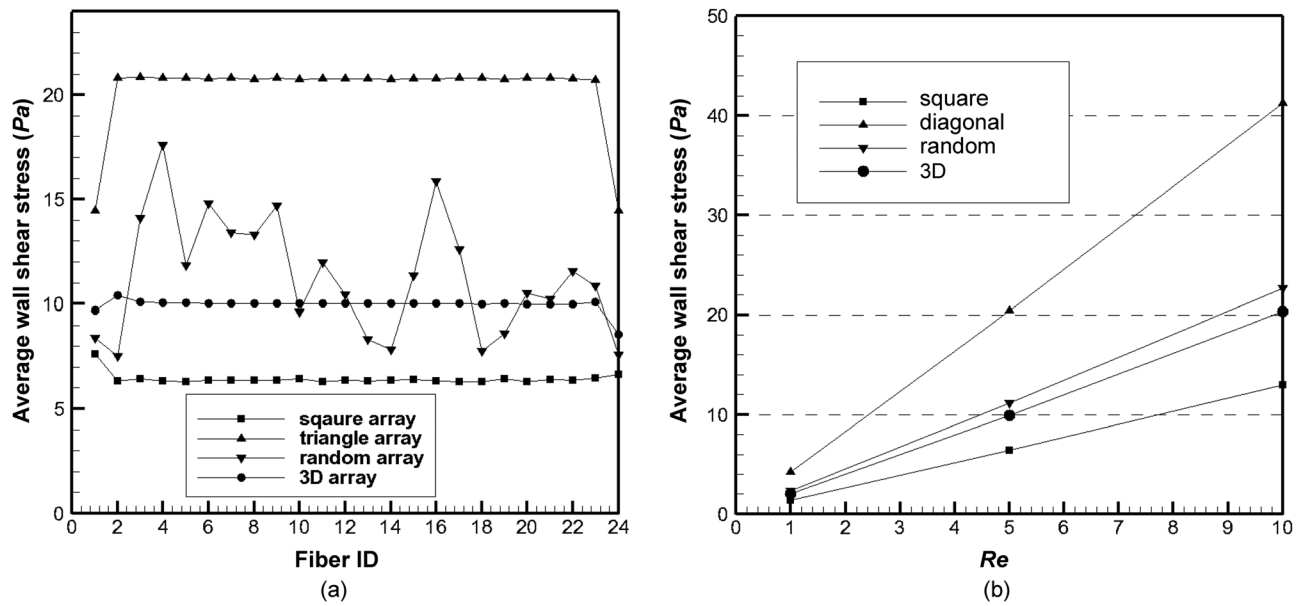

Fig. 8 (*a*) The area-weighted average wall shear stress over individual fibers in a single row along the flow direction when Re is 5.0 and (*b*) the average wall shear stress over all 216 fibers for different Re

term should not be neglected, and the large deviation between the simulation results and the analytical solution is expected.

To correlate the analytical prediction by Eq. (6) with the calculated value by the CFD modeling, a coefficient C for the average wall shear stress can be suggested:

$$\tau_{\text{av\_random}} = C \times \tau_{av} = C\frac{4}{\pi}\frac{\mu_c(Q/A)}{\sqrt{K_p}} \tag{7}$$

Comparing the CFD data with the analytical solution, one can get $C = 1.16$, 1.51, 2.05, and 1.50 for the square, random, diagonal,

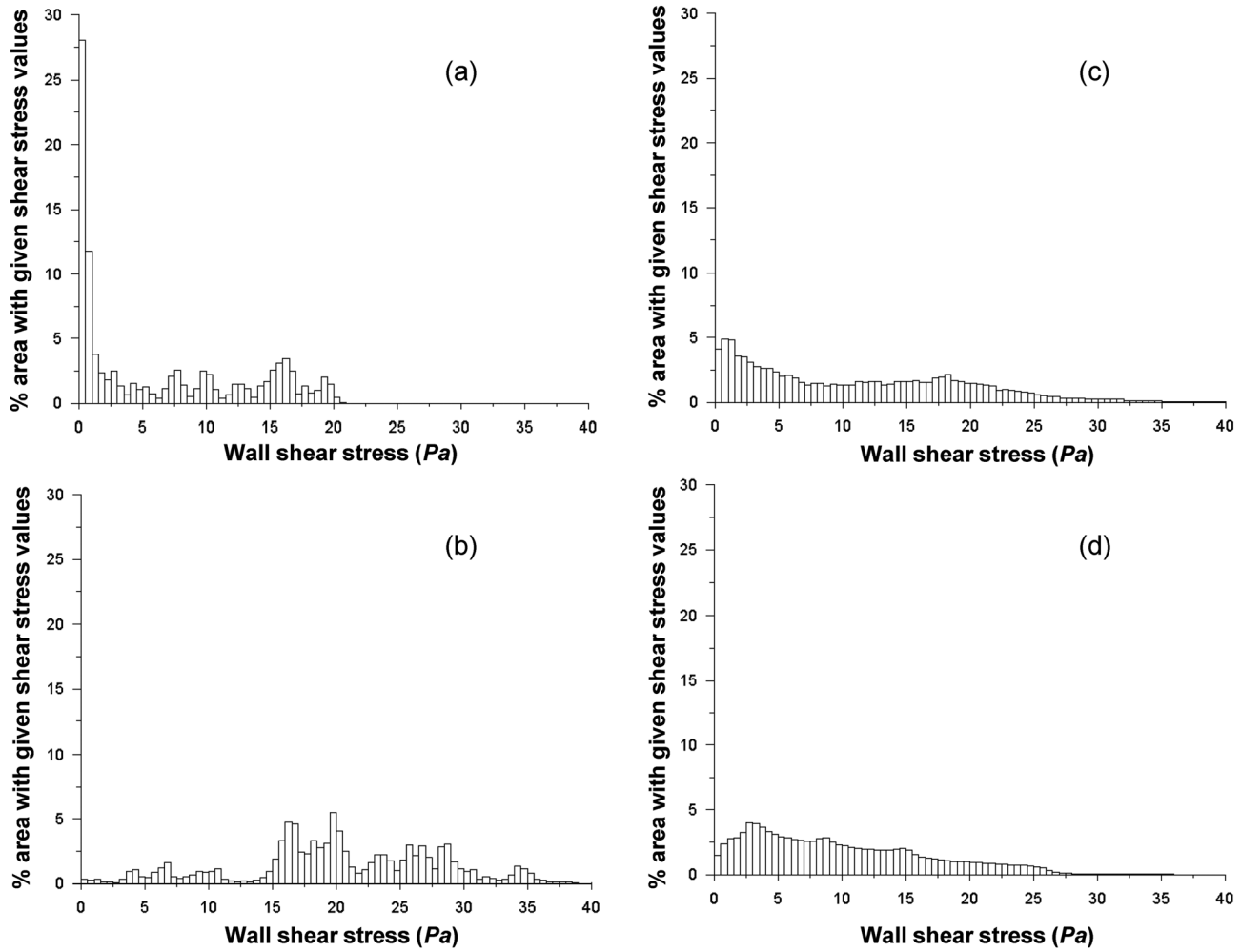

Fig. 9 Probability density function (PDF) of the global wall shear stress over all 216 fibers when Re is 5.0, for the (*a*) square, (*b*) diagonal, (*c*) random, and (*d*) 3D arrays

Table 1 Maximum, median, and mean (area-weighted average) wall shear stress values (Pa) over the total 216 fibers for the square, diagonal, and random arrays

	Re = 1.0			Re = 5.0			Re = 10.0		
	Max	Median	Mean	Max	Median	Mean	Max	Median	Mean
Square	4.36	0.88	1.35	21.80	3.91	6.42	45.86	6.25	12.96
Diagonal	8.97	3.85	4.23	45.98	20.05	20.42	95.56	45.02	41.28
Random	10.27	2.25	2.31	52.58	9.75	11.11	112.94	21.03	22.68
3D	5.25	1.83	2.05	26.93	8.54	9.89	61.69	16.84	20.35

and 3D arrays, respectively. Since C is approximately constant for each type of array, one can conclude that C is not sensitive to the flow field, and it can be treated as a function of the geometric properties only. Wang et al. proposed an analytical solution for the coefficient C for the square array [28]

$$C = \frac{1 - 0319285\varepsilon^2 - 0.043690\varepsilon^4}{\sqrt{(1-\varepsilon-0.305828\varepsilon^4)(1+\varepsilon-0.305828\varepsilon^4)}} + O(\varepsilon^6) \quad (8)$$

where ε is the solid volume fraction of fibers. Given the solid volume fraction of the square array 0.45 in this paper, one can derive $C = 1.06$ from Eq. (8). Although the geometric configurations (i.e., spaces between two neighboring fibers relative to the fiber diameter) of the square fiber array studied by Wang and Tarbell

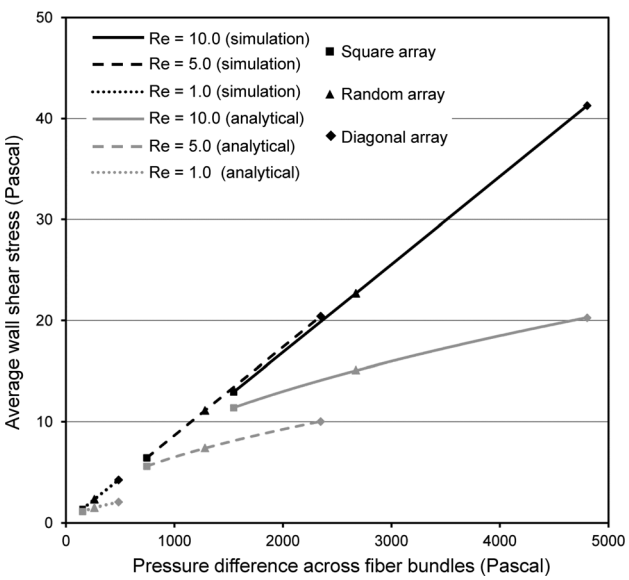

Fig. 10 Simulated average wall shear stress (black lines) of the square (square symbols), diagonal (diamond symbols), and random (triangular symbols) arrays compared with the analytically solutions (gray lines). The simulation results of the three types of arrays are grouped with the same Re, i.e., Re = 1.0 (dotted lines), Re = 5.0 (dashed lines), Re = 10.0 (solid lines).

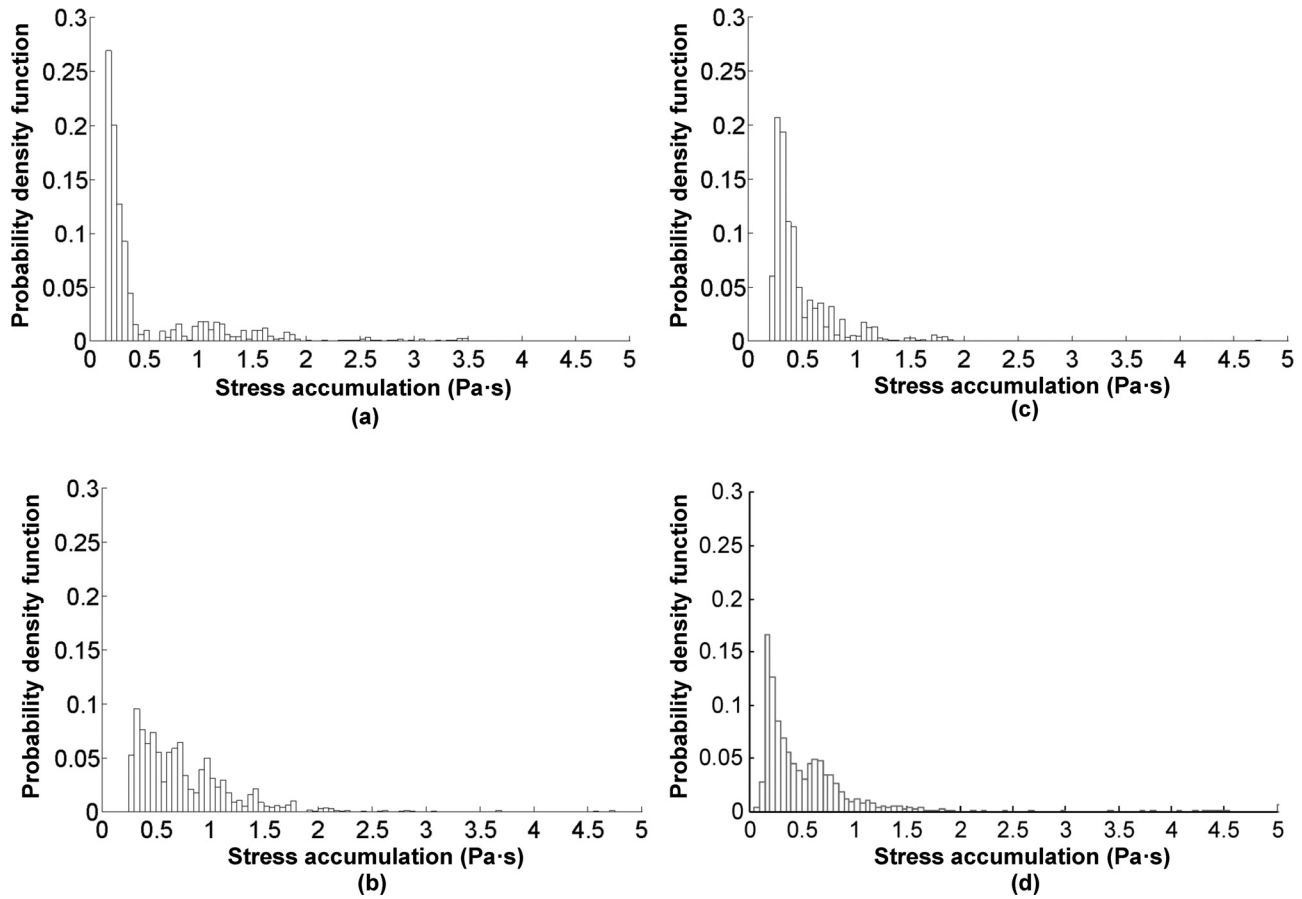

Fig. 11 Probability density function (PDF) of the linear stress accumulation (SA) in the (*a*) square, (*b*) diagonal, (*c*) random and (*d*) 3D arrays when Re is 5.0

[28] differ from those of the square array in this paper, the coefficient calculated from Eq. (8) (1.06) is very close to the value calculated from CFD simulation in this paper (1.16). Considering C is not sensitive to the flow field, one promising way to estimate the fiber-bundle-induced blood damage more precisely is to estimate C by directly simulating a small region of the whole fiber bundle and applying C to the simplified porous media solution on the whole fiber bundle. This could significantly reduce the computational cost of the microscale CFD simulation but largely improve the accuracy of the macroscale porous media simulation.

Three-dimensional effects play an important role in estimating shear-induced blood damage. Very often, fiber bundles are treated as two-dimensional uniformly arranged arrays for CFD model constructions in order to reduce the cost [14–20]. In this study, significant variances in velocity, shear rate, and wall shear stress fields are observed in z direction in the 3D array (see Fig. 3 and Fig. 6). 3D array and random array have similar average wall shear stress and SA distribution, which indicates that the average hemolysis and platelet activation due to mechanical shear are approximately comparable in these two arrays. However, since initiation of platelet deposition and aggregation is significantly affected by local blood flow disturbances [40], platelet deposition could be significantly different in 3D arrays.

Steady flow is applied in this study. However, blood flow from the right heart ventricle is pulsatile, which peak velocity, pressure, and shear stress could be several times higher. Additionally, Sheriff et al. reported that platelet activation is significantly affected by shear loading rate [41], which implies that acceleration and deceleration in blood flow may cause more damage than constant shear stress. It is apparent that platelet activation and deposition in time-dependent flow could be notably different from in steady state flow. However, the aim of this study is to develop a microscale CFD modeling approach to understand blood flow in hollow fiber bundles for artificial lung devices and hemodialyzers more precisely. In other words, the relationship between shear stress distribution and the geometric properties of different types of fiber arrays is the primary interest of this paper. Furthermore, Zierenberg et al. reported that oxygenators are recommended to be operated at near steady state in order to achieve optimal hemodynamic and gas exchange characteristics [17]. Thus, steady state flow seems to be a reasonable choice for this study.

5 Conclusion

Blood flow with different Re through square, diagonal, and random and 3D fiber arrays with the same porosity are studied in this paper. The local shear stress is found to vary significantly in these arrays. Simulated shear stresses in these arrays are well below the threshold causing hemolysis, and the exposure time was not long either. In other words, hemolysis is negligible inside fiber arrays. However, the platelet activation due to mechanical shear stress and the platelet deposition may exist for these arrays. For each of these arrays, the area-weighted average wall shear stress increases linearly with the Re, and the simulated global average wall shear stresses are larger than the analytical predictions. Furthermore, the average wall shear stress of different types of arrays with the same Re also increases linearly with the pressure difference across arrays, which significantly deviated from the power-law model analytically predicted. A coefficient C is suggested to correlate the analytical porous media prediction and the simulation data and can be used to improve the accuracy of the homogeneous porous media prediction. Specifically, C is 1.16, 1.51, 2.05, and 1.50 for the square, random, diagonal, and 3D arrays in this study, respectively. This study shows that C does not change with Re but varies

with the array type, which indicates that C is strongly dependent on the array geometrical properties, such as fiber diameter and porosity, and is weakly correlated with the flow field. Additionally, the average wall shear stress of the 3D array is similar as that of the random array. Shear stress in the diagonal array and square array may be used as the upper and lower limits in evaluating blood damage in fiber bundles. Further study is necessary to understand the relationship between the average wall shear stress and other geometrical properties (i.e., the fiber diameter and the angle between fibers).

Acknowledgment

This study was supported in part by the National Institutes of Heath (Grant Numbers R42 HL084807, R01HL082631).

References

[1] Haft, J. W., Griffith, B. P., Hirschl, R. B., and Bartlett, R. H., 2002, "Results of an Artificial-Lung Survey to Lung Transplant Program Directors," J. Heart Lung Transplant, **21**(4), pp. 467–473.
[2] Zhang, J., Nolan, T. D. C., Zhang, T., Griffith, B. P., and Wu, Z. J., 2007, "Characterization of Membrane Blood Oxygenation Devices Using Computational Fluid Dynamics," J. Memb. Sci., **288**, pp. 268–279.
[3] Zhang, J., Taskin, M. E., Koert, A., Zhang, T., Gellman, B., Dasse, K. A., Gilbert, R. J., Griffith, B. P., and Wu, Z. J., 2009, "Computational Design and in Vitro Characterization of an Integrated Maglev Pump Oxygenator," Artif. Organs, **33**(10), pp. 805–817.
[4] Bloembergen, W. E., Stannard, D. C., Port, F. K., Wolfe, R. A., Pugh, J. A., Jones, C. A., Greer, J. W., Golper, T. A., and Held, P. J., 1996, "Relationship of Dose of Hemodialysis and Cause-Specific Mortality," Kidney Int., **50**(2), pp. 557–565.
[5] Matsuda, N., Nakamura, M., Sakai, K., Kuwana, K., and Tahara, K., 1999, "Theoretical and Experimental Evaluation for Blood Pressure Drop and Oxygen Transfer Rate in Outside Blood Flow Membrane Oxygenator," J. Chem. Eng. Jap., **32**(6), pp. 752–759.
[6] Matsuda, N., and Sakai, K., 2000, "Blood Flow and Oxygen Transfer Rate of an Outside Blood Flow Membrane Oxygenator," J. Memb. Sci., **170**(2), pp. 153–158.
[7] Dierickx, P. W., De Wachter, D. S., De Somer, F., Van Nooten, G., and Verdonck, P. R., 2001, "Mass Transfer Characteristics of Artificial Lungs," ASAIO J., **47**(6), pp. 628–633.
[8] Wickramasinghe, S. R., Garcia, J. D., and Han, B., 2002, "Mass and Momentum Transfer in Hollow Fibre Blood Oxygenators," J. Memb. Sci., **208**(1–2), pp. 247–256.
[9] Gartner, M. J., Wilhelm, C. R., Gage, K. L., Fabrizio, M. C., and Wagner, W. R., 2000, "Modeling Flow Effects on Thrombotic Deposition in a Membrane Oxygenator," Artif. Organs, **24**(1), pp. 29–36.
[10] Gage, K. L., Gartner, M. J., Burgreen, G. W., and Wagner, W. R., 2002, "Predicting Membrane Oxygenator Pressure Drop Using Computational Fluid Dynamics," Artif. Organs, **26**(7), pp. 600–607.
[11] Funakubo, A., Taga, I., McGillicuddy, J. W., Fukui, Y., Hirschi, R. B., and Bartlett, R. H., 2003, "Flow Vectorial Analysis in an Artificial Implantable Lung," ASAIO J., **49**(4), pp. 383–387.
[12] Sato, H., Taga, I., Kinoshita, T., Funakubo, A., Ichiba, S., and Shimizu, N., 2006, "In Vitro Evaluation of a Newly Developed Implantable Artificial Lung," Acta Med. Okayama, **60**(2), pp. 113–119.
[13] Zinovik, I. N., and Federspiel, W. J., 2007, "Modeling of Blood Flow in a Balloon-Pulsed Intravascular Respiratory Catheter," ASAIO J., **53**(4), pp. 464–468.
[14] Zierenberg, J. R., Fujioka, H., Suresh, V., Bartlett, R. H., Hirschl, R. B., and Grotberg, J. B., 2006, "Pulsatile Flow and Mass Transport Past a Circular Cylinder," Phys. Fluids, **18**(1), pp. 1–15.
[15] Zierenberg, J. R., Fujioka, H., Hirschl, R. B., Bartlett, R. H., and Grotberg, J. B., "Pulsatile Flow and Mass Transport Past a Circular Cylinder," ASME J. Biomech. Eng., **129**(2), pp. 202–215.
[16] Chan, K. Y., Fujioka, H., Suresh, V., Bartlett, R. H., Hirschl, R. B., and Grotberg, J. B., 2006, "Pulsatile Flow and Mass Transport Over an Array of Cylinders: Gas Transfer in a Cardiac-Driven Artificial Lung," ASME J. Biomech. Eng., **128**(1), pp. 85–96.
[17] Zierenberg, J. R., Fujioka, H., Cook, K., and Grotberg, J. B., 2008, "Pulsatile Flow and Oxygen Transport Past Cylindrical Fiber Arrays for an Artificial Lung: Computational and Experimental Studies," ASME J. Biomech. Eng., **130**(3), pp. 1–12.
[18] Dierickx, P. W., de Wachter, D. S., and Verdonck, P. R., 2001, "Two-Dimensional Finite Element Model for Oxygen Transfer in Cross-Flow Hollow Fiber Membrane Artificial Lung," Int. J. Artif. Organs, **24**(9), pp. 628–635.
[19] Mazaheri, A. R., and Ahmadi, G., 2006, "Uniformity of the Flow Velocities Within Hollow Fiber Membranes of Blood Oxygenation Devices," Artif. Organs, **30**(1), pp. 10–15.
[20] Taskin, M. E., Fraser, K. H., Zhang, T., Griffith, B. P., and Wu, Z. J., 2010, "Micro-Scale Modeling of Flow and Oxygen Transfer in Hollow-Fiber Membrane Bundle," J. Memb. Sci., **362**(1–2), pp. 172–183.
[21] Nagase, K., Kohori, F., and Sakai, K., 2005, "Oxygen Transfer Performance of a Membrane Oxygenator Composed of Crossed and Parallel Hollow Fibers," Biochem. Eng. J., **24**(2), pp. 105–113.
[22] Zierenberg, J. R., Fujioka, H., Hirschl, R. B., Bartlett, R. H., and Grotberg, J. B., 2009, "Oxygen and Carbon Dioxide Transport in Time-Dependent Blood Flow Past Fiber Rectangular Arrays," Phys. Fluids, **21**(3), p. 033101.
[23] Bodnar, T., Sequeira, A., and Prosi, M., 2011, "On the Shear-Thinning and Viscoelastic Effects of Blood Flow Under Various Flow Rates," Appl. Math. Comput., **217**(11), pp. 5055–5067.
[24] Chen, J., Lu, X. Y., and Wang, W., 2006, "Non-Newtonian Effects of Blood Flow on Hemodynamics in Distal Vascular Graft Anastomoses," J. Biomech., **39**(11), pp. 1983–1995.
[25] Gonzalez, H. A., and Moraga, N. O., 2005, "On Predicting Unsteady Non-Newtonian Blood Flow," Appl. Math. Comput., **170**(2), pp. 909–923.
[26] Cioffi, M., Boschetti, F., Raimondi, M. T., and Dubini, G., 2006, "Modeling Evaluation of the Fluid-Dynamic Microenvironment in Tissue-Engineered Constructs: A Micro-CT Based Model," Biotechnol. Bioeng. **93**(3), pp. 500–510.
[27] Wang, S., and Tarbell, J. M., 2000, "Effect of Fluid Flow on Smooth Muscle Cells in a 3-Dimensional Collagen Gel Model," Arterioscler., Thromb., Vasc. Biol., **20**(10), pp. 2220–2225.
[28] Wang, D. M., and Tarbell, J. M., 1995, "Modeling Interstitial Flow in an Artery Wall Allows Estimation of Wall Shear Stress on Smooth Muscle Cells," ASME J. Biomech. Eng., **117**(3), pp. 358–363.
[29] Xenos, M., Girdhar, G., Alemu, Y., Jesty, J., Slepian, M., Einav, S., and Bluestein, D., 2010, "Device Thrombogenicity Emulator (DTE)—Design Optimization Methodology for Cardiovascular Devices: a Study in Two Bileaflet MHV Designs," J. Biomech., **43**(12), pp. 2400–2409.
[30] Leverett, L. B., Hellums, J. D., Alfrey, C. P., and Lynch, E. C., 1972, "Red Blood Cell Damage by Shear Stress," Biophys. J., **12**(3), pp. 257–273.
[31] Giersiepen, M., Wurzinger, L. J., Opitz, R., and Reul, H., 1990, "Estimation of Shear Stress-Related Blood Damage in Heart Valve Prosthesis – in Vitro Comparison of 25 Aortic Valves," Int. J. Artif. Organs, **13**(5), pp. 300–306.
[32] Fraser, K. H., Zhang, T., Taskin, M. E., Griffith, B. P., and Wu. Z. J., 2012, "A Quantitative Comparison of Mechanical Blood Damage Parameters in Rotary Ventricular Assist Devices: Shear Stress, Exposure Time and Hemolysis Index," ASME J. Biomech. Eng., **134**(8), p. 081002.
[33] Wu, Z. J., Taskin, M. E., Zhang, T., Fraser, K. H., and Griffith, B. P., 2012, "Computational Model-Based Design of a Wearable Artificial Pump-Lung for Cardiopulmonary/Respiratory Support," Artif. Organs, **36**(4), pp. 387–399.
[34] Fill, B., Gartner, M., Johnson, G., Horner, M., and Ma, J., 2008, "Computational Fluid Flow and Mass Transfer of a Functionally Integrated Pediatric Pump-Oxygenator Configuration," ASAIO J., **54**(2), pp. 214–219.
[35] Apel, J., Paul, R., Klaus, S., Siess, T., and Reul, H., 2001, "Assessment of Hemolysis Related Quantities in a Microaxial Blood Pump by Computational Fluid Dynamics," Artif. Organs, **25**(5), pp. 341–347.
[36] De Wachter, D., and Verdonck, P., 2002, "Numerical Calculation of Hemolysis Levels in Peripheral Hemodialysis Cannulas," Artif. Organs, **26**(7), pp. 576–582.
[37] Ichinose, K., Okamoto, T., Tanimoto, H., Yoshitake, A., Tashiro, M., Sakanashi, Y., Kuwana, K., Tahara, K., Kamiya, M., and Terasaki, H., 2004, "Comparison of a New Heparin-Coated Dense Membrane Lung With Nonheparin-Coated Dense Membrane Lung for Prolonged Extracorporeal Lung Assist in Goats," Artif. Organs, **28**(11), pp. 993–1001.
[38] Chan, K. Y., Fujioka, H., Hirshl, R. B., Bartlett, R. H., and Grotberg J. B., 2007, "Pulsatile Blood Flow and Gas Exchange Across a Cylindrical Fiber Array," ASME J. Biomech. Eng., **129**(5), pp. 676–687.
[39] Cioffi, M., Boschetti, F., Raimondi, M. T., and Dubini, G., 2006, "Modeling Evaluation of the Fluid-Dynamic Microenvironment in Tissue-Engineered Constructs: A Micro-CT Based Model," Biotechnol. Bioeng., **93**(3), pp. 500–510.
[40] Schoephoerster, R. T., Oynes, F., Nunez, G., Kapadvanjwala, M., and Dewanjee, M. K., 1993, "Effects of Local Geometry and Fluid Dynamics on Regional Platelet Deposition on Artificial Surfaces," Arterioscler Thromb., **13**(12), pp. 1806–1813.
[41] Sheriff, J., Soares, J. S., Xenos, M., Jesty, J., and Bluestein, D., 2013, "Evaluation of Shear-Induced Platelet Activation Models Under Constant and Dynamic Shear Loading Conditions Relevant to Devices," Ann Biomed Eng., **41**(6), pp. 1279–1296.